Wear 544–545 (2024) 205268

Contents lists available at ScienceDirect

Wear

journal homepage: www.elsevier.com/locate/wear

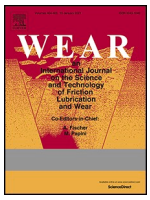

Discrete element modelling of rolling contact fatigue and crack closure with different bond laws

Markus Januschewsky [a,b,*], Gerald Trummer [a], Klaus Six [a], Roger Lewis [b]

[a] Virtual Vehicle Research GmbH, Inffeldgasse 21a, 8010 Graz, Austria
[b] The University of Sheffield, Department of Mechanical Engineering, Engineering Heartspace, Sir Frederick Mappin Building, Mappin Street, Sheffield S1 3JD, UK

ARTICLE INFO

Keywords:
Wheel-rail contact
Rolling contact fatigue
Fatigue crack growth
Discrete element method
Peridynamic modelling
Crack closure
Bond law

ABSTRACT

The prediction of rolling contact fatigue requires modelling methods that efficiently simulate the propagation, branching and coalescence of fatigue cracks. The developed Discrete Element Method (DEM) model is a novel approach to provide this capability. The model is based on discrete elements (bonds) that are subject to a fatigue law. With it, the failure of elements due to cyclic loads can be simulated. The propagating cracks are not confined to predefined paths, but develop according to the local loading conditions. These conditions depend on an appropriate set-up of the element interaction, i.e. the bond law, which is calibrated, taking into account crack closure effects. The method delivers a relevant improvement for DEM- and peridynamic models, where compressive loads dominate. The current development of the model is summarised in this paper.

1. Introduction

Railway operation is characterised by high loads in compression and shear within the wheel-rail contact. This causes different forms of rail and wheel degradation, i.e. rolling contact fatigue (RCF) related macroscopic cracks and wear. The fatigue development is influenced by severe plastic deformation (SPD) [1], which promotes an anisotropic crack growth behaviour at the contact surface [2]. These degradations cause maintenance costs, as they require inspections and repair, and they potentially compromise safety. Due to the complex conditions in the wheel-rail interface, i.e. contact geometries and stresses, slip, third body layer, the interaction between these degradation phenomena is not yet fully understood.

State of the art for the modelling of solid mechanics is the finite element method (FEM). Regarding fatigue modelling, however, FEM is limited by the basic assumption of having a continuum, which is violated by a discontinuum like a crack. In order to overcome this limitation, the extended FEM (XFEM) was developed, which though requires additional criteria to describe the crack growth behaviour (crack growth rate, direction, coalescence, branching) [3]. This makes it challenging to simulate multiple cracks efficiently. Alternative solutions to investigate fatigue cracks in simulations are discrete approaches like discrete element methods, peridynamics or lattice spring models. These alternatives, however, are used primarily to simulate cases where tension loads are dominant. For the modelling of RCF, peridynamic models are employed at an early stage. A key issue of these approaches regards the mechanical characteristic of failed bonds [4], which is addressed in this paper.

The DEM method was initially developed to model granular materials [5], and was extended to model continuous materials like composites [6]. In this paper, a 2D truss-like DEM model is developed to efficiently model RCF cracks in rails. The core of the model is the layout of the bond law, which is reviewed in Section 2. The bond law is assessed with regard to the compressive loads associated to the wheel-rail contact. The elastic characteristic of the model is set up and the stress field is evaluated in Section 3. Then, initial cracks are introduced, and the resulting stress field is analysed. The next step is the introduction of a fatigue crack growth (FCG) capability in Section 4, in order to facilitate crack growth due to cyclic loading. The initial results of RCF modelling are presented and compared to experimental results in Section 5. In order to overcome discrepancies revealed by the comparison, crack closure effects must be considered and captured by the bond law. Based on experimental results, the bond law is calibrated in Section 6. Finally, the set-up is applied to an RCF simulation and discussed in Section 7.

2. Bond law

The DEM model was derived from the 3D design of Kosteski et al. [7].

* Corresponding author.Virtual Vehicle Research GmbH, Inffeldgasse 21a, 8010 Graz, Austria
E-mail address: markus.januschewsky@v2c2.at (M. Januschewsky).

https://doi.org/10.1016/j.wear.2024.205268
Received 28 February 2023; Received in revised form 16 January 2024; Accepted 19 January 2024
Available online 6 February 2024

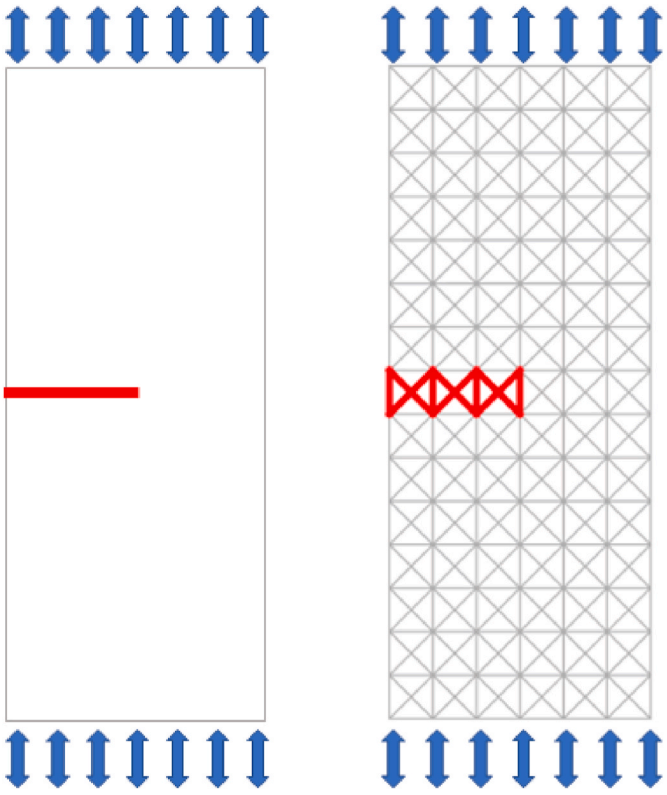

Fig. 1. Cracked specimen (crack in red) that is loaded in tension and compression: Continuous model (left) and DEM model (right). For the latter, the crack is illustrated by failed bonds coloured in red. (For interpretation of the references to colour in this figure legend, the reader is referred to the Web version of this article.)

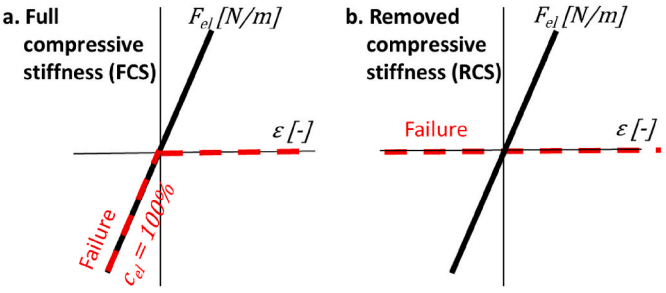

Fig. 2. Bond law set-ups: The law for healthy elements is coloured in black, the one for failed elements dashed in red. The bond law with full compressive stiffness for failed elements is displayed in figure a, the standard bond law from the literature with no compressive stiffness is displayed in b. (For interpretation of the references to colour in this figure legend, the reader is referred to the Web version of this article.)

The model consists of nodes that are positioned in a square arrangement. Generally, all nodes are connected to eight adjacent nodes via discrete elements (bonds), which forms a truss-like arrangement (see Fig. 1, right). Each squared truss represents a DEM module. All elements can be loaded in the axial direction only, buckling is neglected. There are no explicit shear elements. A shear load applied to the grid is supported by elements that have a relative orientation of $\pm$ 45° to the surface edge, i.e. these elements are diagonally oriented with respect to the surface. These elements provide a shear stiffness to the model [7]. In this way, shear stresses are captured (see section 3). A state of plain strain is assumed. Dynamic effects are omitted.

The mechanical characteristic of the model is defined by the constitutive strain-force-relation of a bond, i.e. the bond law, which applies to all elements regardless of their orientation. This agrees with the modelling approach applied in peridynamics [8]. The strain ε for state "1" is defined by the change of element length Δl with respect to the initial length l_0 at state "0".

$$\varepsilon = \frac{(l_1 - l_0)}{l_0} = \frac{\Delta l}{l_0} \qquad \text{Equation 1}$$

The element force F_{el} is the response to a strain ε.

$$F_{el} = c_{el} * \varepsilon \qquad \text{Equation 2}$$

The bond law must capture the behaviour for two cases, i.e. for healthy- and failed elements. The two cases are differentiated by a damage variable, which is introduced in Section 4 (see Fig. 13). When the damage variable reaches a specific value, the element's state is set from healthy to failed, which is detailed in Section 4. Concerning the first case, a linear-elastic material behaviour is assumed (see Equation (2)) and a corresponding bond law is assigned to all healthy elements (see Fig. 2a and b). The elasticity parameter c_{el} is the only parameter required to establish the bond law for healthy elements.

The main benefit of the model is that cracks can be integrated in a simple way, i.e. by the failure of bonds. This eases the modelling of FCG and permits the simulation of multiple cracks. The failure of a bond is introduced by a bond fatigue law in combination with the modification of the associated bond law.

The key question is "how do elements behave in the case of failure?". Therefore, a specimen with a crack perpendicular to the longitudinal axis is compared to a corresponding DEM model (see Fig. 1). If a tensile load is applied to the specimen, only the uncracked cross section will carry load, whereas the cracked part will not. This implies for the model that failed elements (see Fig. 1, right, red elements) cannot bear a tensile load (see Fig. 2a and b, right quadrants, $\varepsilon > 0$).

If a compressive load is applied, the specimen (see Fig. 1, left) is expected to respond in a comparable way to an uncracked part. Regarding the model's bond law, this requires a stiff, non-zero response for failed elements loaded in compression, i.e. $\varepsilon < 0$. Initially, the stiffness of healthy elements was adopted to failed elements, constituting a "full compressive stiffness" bond law (FCS, see Fig. 2a, left quadrants).

In the literature about DEM- and peridynamic models, a different approach was adopted as a standard set-up. In the works of Kosteski et al. [7] and Silling and Askari [8], which focus primarily on the modelling of tensile loading states, the failure of an element corresponds to a complete loss of load carrying capability. The set-up is referred to as "removed compressive stiffness" bond law (RCS, see Fig. 2b, left quadrants).

The disadvantage of this bond law is that a model with a crack loaded in compression (see Fig. 1, right) behaves in a non-physical way as the crack is squeezed. This may lead to excessive deformation of the grid around the crack, or to an interpenetration of the crack faces as the crack is completely soft. For most engineering applications, where tensile loadings prevail, this effect is not relevant. However, for the modelling of a rolling contact, where compressive loads have a dominant influence, this characteristic poses a serious shortcoming, which was highlighted by Freimanis and Kaewunruen [4].

In order to tackle the issue of interpenetration, Silling and Askari proposed contact models, i.e. the introduction of "short-range repulsive forces" that are "independent of the positions of the nodes" to counter the potential contact of crack faces [9]. In this model, however, only small node deformations are assumed, which makes the stiffening of failed elements under compressive strain a more appropriate solution. With respect to RCF modelling, also Ghaffari et al. acknowledged the requirement to retain a stiffness for failed bonds loaded in compression [10,11]. This was performed by a reduction of the original element elasticity. Unfortunately, they did not specify or discuss the modification.

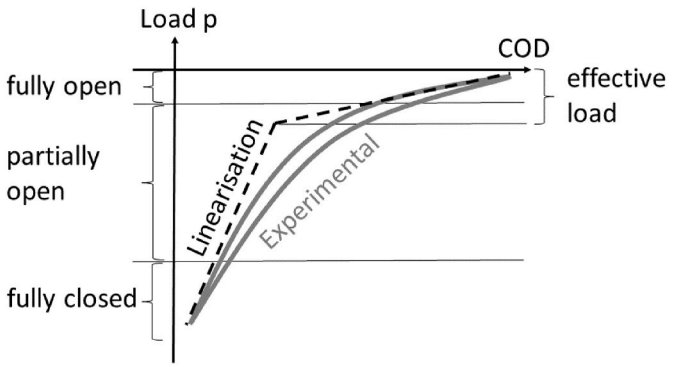

Fig. 3. Load-crack opening displacement (COD) curves of FCG tests, modified from Ref. [12]: The experimental results are illustrated in grey, the simplification in dashed black.

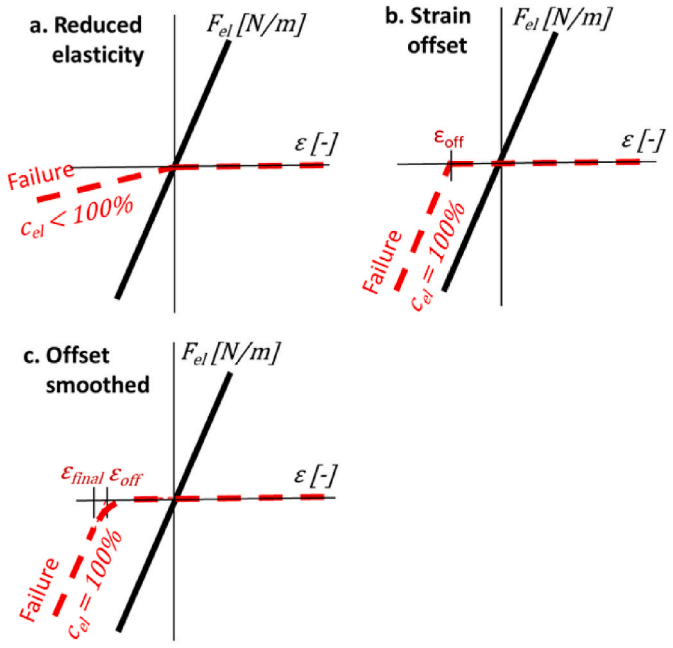

Fig. 4. Alternative bond law set-ups: The law for healthy elements is coloured in black, the one for failed elements dashed in red. (For interpretation of the references to colour in this figure legend, the reader is referred to the Web version of this article.)

An alternative approach to answer the question of how a cracked material responds to an applied compressive load (see Fig. 1) is provided by the experimental work of Kasaba et al. [12]. They performed FCG tests on pre-deformed austenitic steel specimens under pure compressive loads, $p < 0$, and measured the crack opening displacement (COD) (see Fig. 3). By COD, the crack mouth opening displacement (CMOD) is meant, which characterises the displacement of the two crack faces at the crack's mouth [13]. The higher the applied compressive load, p, the more the crack is closed, and thus COD reduces (see Fig. 3). In this way, the effect of crack closure can be measured, i.e. the interaction of the crack faces that retards the opening and closure of cracks. This effect is expected to occur for pearlitic rail steels as well. Kasaba et al. approximated the COD behaviour by a linearisation to define an effective load at which the crack grows.

With respect to the stated question, this simplification suggests that a cracked specimen under compression (see Fig. 1) exhibits a reduced stiffness when the crack is fully or partially open. For an increase of the applied compressive load, p, the crack closes, and a transition to full stiffness occurs (see Fig. 3, linearisation).

Considering the closure behaviour of a DEM model (see Fig. 1, right) with the discussed bond laws (see Fig. 2a–b), a model with the FCS bond law is expected to transition to full stiffness, i.e. the crack is fully closed, at an applied load (effective load) of around zero. This contrasts with the experimental observations (see Fig. 3). A model with the RCS bond law is assumed to have no transition at all, as the failed elements are effectively removed. As a result, none of the two bond laws can capture the observed COD behaviour. Though, the latter provides a reference for alternative bond law set-ups. In this paper, alternative bond law set-ups were investigated that encompass a reduced elasticity (see Fig. 4a), a strain offset (see Fig. 4b) or a smoothed offset (see Fig. 4c). The proposed set-ups serve for the modelling of the macro-mechanical crack closure behaviour observed in the experiment (see Fig. 3). They are not associated to a specific physical effect.

In addition to the mechanical response of a crack loaded in compression, the shear interaction of the crack faces is relevant for an RCF application. With regard to the alternative bond law set-ups (see Fig. 4), this effect can be captured partially. A shear load causes tensile and compressive strains in the diagonally oriented bonds. The bonds loaded in compression facilitate some shear interaction across the crack surfaces. At the initial stage of the model development, this characteristic is considered to be sufficient.

In summary, there are different possibilities to set up the bond law to model a crack loaded in compression. For the next step of modelling a rolling contact with a surface crack, the FCS bond law (see Fig. 2a) was selected as set-up.

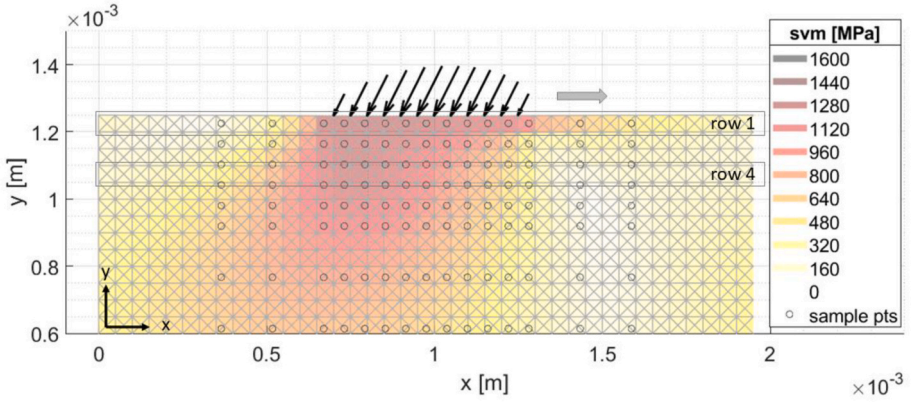

Fig. 5. Rolling contact simulation with stress distribution σ_{VM} for an undamaged case. For the parameterisation, a sampling grid in a range of [± 2 A] in width and [0–2 A] in depth with respect to the semi contact length, A, is used (see grid of black dots).

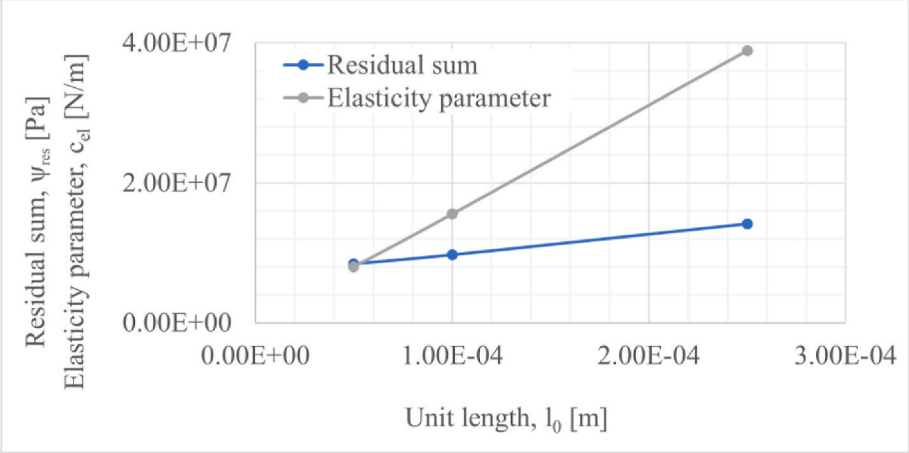

Fig. 6. Elasticity parameter, c_{el}, and residual sum, ψ_{res}, as a function of the element's unit length, l_0.

3. Stress field around initial cracks

The DEM model was developed primarily to model RCF. It is implemented in MatLab® programming language. The load applied to the model surface was modelled as a semi-elliptic pressure distribution p (x) representing a Hertzian normal contact. For the tangential load τ(x), full sliding and thus a semi-elliptic stress distribution were assumed. The stress distributions were approximated by equivalent forces that were applied to the nodes (see Fig. 5). A periodic boundary condition was applied in the rolling direction. An optimisation routine was employed to minimise the sum of the forces in the nodes. The outcome was a set of node coordinates, which was used as an input for the next increment. In this way, a rolling contact was modelled by a series of quasi-static increments.

In order to calculate a stress distribution, the approach of Kosteski et al. [7] was adopted to transform element forces into module based stresses. In this way, the stress tensor for a plane strain condition was post-processed per DEM module. The strain tensor was not post-processed, because the fatigue behaviour is determined by bond strains (see section 4). Further, an equivalent von Mises stress σ_{VM} was calculated.

For parametrisation, the elasticity parameter c_{el} (see Equation (2)) was derived by an optimisation and applied to all healthy bonds (gradient in Figs. 2 and 4). As an analytical reference, the stress distribution for Hertzian normal contact and full sliding in tangential direction (assuming a coefficient of friction μ) was adopted from Johnson [14]. With it, the equivalent stress distribution was calculated for a specific grid of sampling points ([± 2 A] in width and [0–2 A] in depth with respect to the semi contact length, A, see Fig. 5). These reference values were compared to the interpolated and sampled results (see sampling grid, Fig. 5) of the model. For both, the reference and the model results, a vector was defined that captured the stresses, σ_{VM}, of all sampling points. The error between the two vectors was calculated and squared (vector of residuals). Finally, the residuals were summed, the square root was taken and divided by the number of sampling points to derive a residual sum, ψ_{res}. The residual sum was minimised by the optimisation to derive the elasticity parameter, c_{el}, of the bonds.

For a reference case with a Hertzian load and a maximum contact normal stress, p_0 of 1500 MPa, the residual sum, ψ_{res}, was minimised for different grid discretisations. The result of the study revealed that the elasticity parameter, c_{el}, decreases with the element size, l_0, in a linear way (see Fig. 6). In this way, the optimum elasticity was set for different grid discretisations. The study proved that the residual sum, ψ_{res}, converged with a refinement of the grid (see Fig. 6). Due to the refined grid, the stress field resolution improved. The remaining error was attributed predominantly to the model's inherent limitation to a Poisson ratio of $\nu = 0.25$, which is detailed by Silling et al. [15].

A case with initial cracks at three distinct positions is displayed in Fig. 7. One crack is behind the contact (crack #1), a second one in the centre (crack #2) and a third one in front of it (crack #3). The crack paths have an orientation of 45° with respect to the surface. A normal stress of $p_0 = 1500$ MPa was applied and a coefficient of friction, μ of 0.5 was assumed. The FCS bond law (see Fig. 2a) was applied to failed elements to model the cracks. Regarding the shear interaction of opposite crack faces, the FCS bond law implied that a crack behaved similar to an uncracked material, which corresponded to a wedging of crack faces. Thus, crack face friction was not considered.

Figs. 5, Figs. 8 and 10 display results for the undamaged case, while

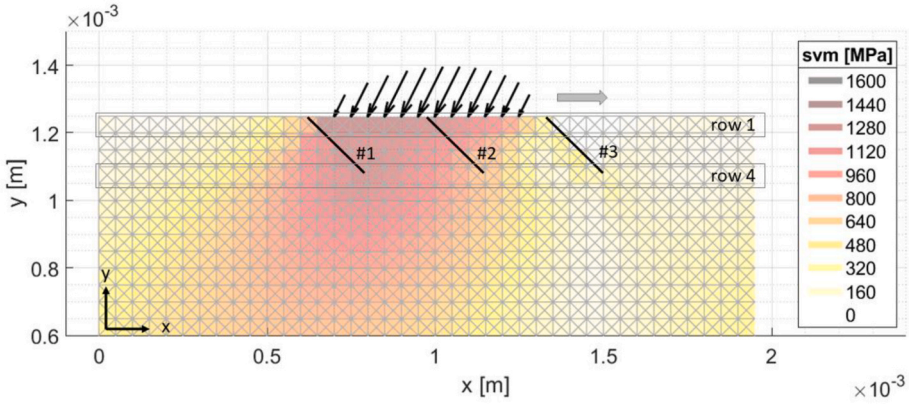

Fig. 7. Rolling contact simulation with stress distribution σ_{VM} that is subject to three surface cracks (displayed in black).

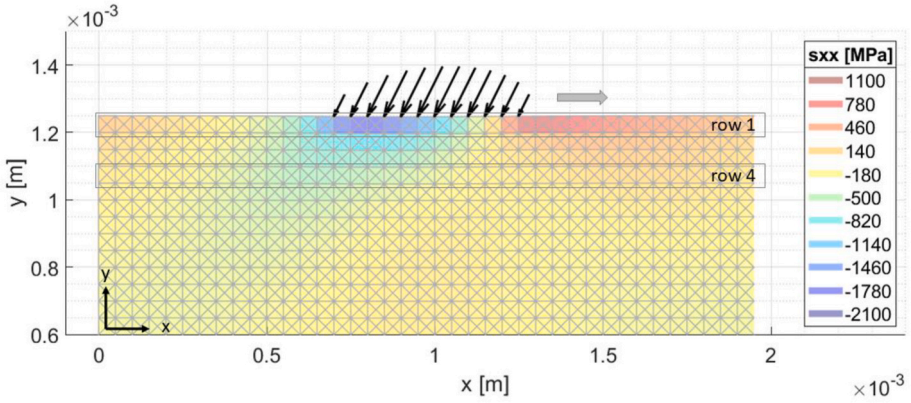

Fig. 8. Rolling contact simulation with stress distribution σ_{xx} for an undamaged case.

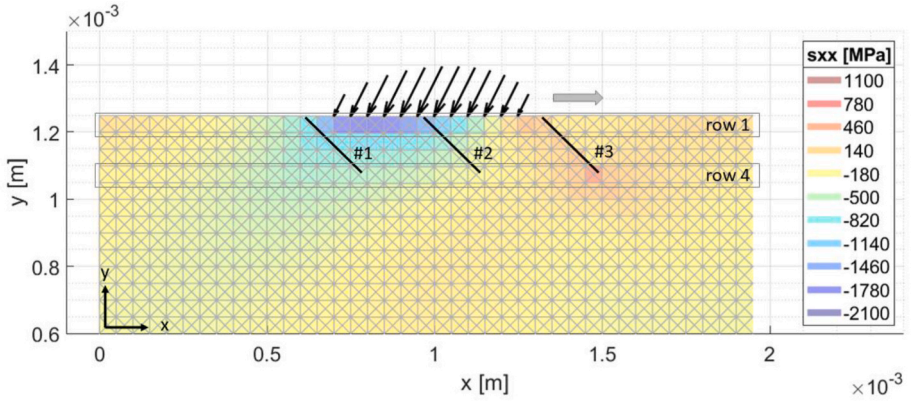

Fig. 9. Rolling contact simulation with stress distribution σ_{xx} that is subject to three surface cracks (displayed in black).

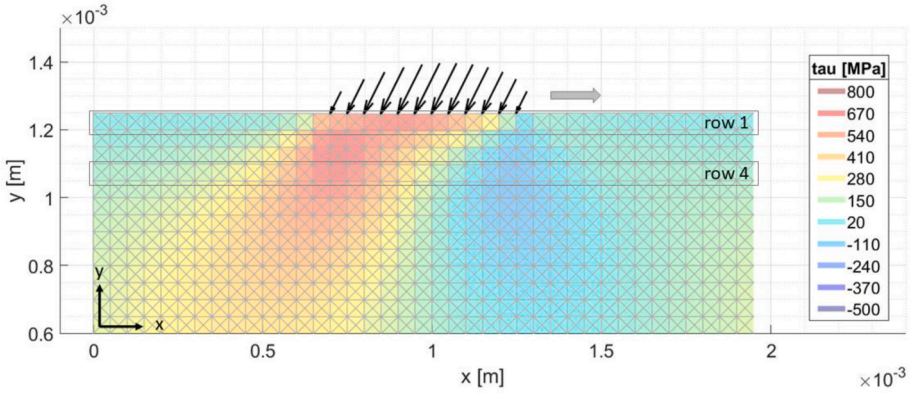

Fig. 10. Rolling contact simulation with shear stress distribution τ_{xy} for an undamaged case.

Figs. 7, Figs. 9 and 11 show results for a case with three cracks. Fig. 12 compares the distributions of the stress σ_{xx} for the two cases. The cracks to the left of and below the contact (#1, #2) do not affect the stress field significantly as the failed bonds in this area are predominantly loaded in compression. Due to the applied FCS bond law (see Fig. 2a), the bonds can transmit forces in this case. However, the righthand crack (#3) has a significant impact on the σ_{VM} stress field, which is because of the tensile loading in the area.

An analysis of the stress distribution σ_{xx} highlights this loading condition for the undamaged case, primarily on the surface (see Fig. 8, module row 1). For the damaged case, the maximum tensile stress σ_{xx} on the surface decreases (see Fig. 9, row 1). A closer look on the surface reveals a stress decrease before and a drop to zero after the crack (see Fig. 12, row 1).

In the subsurface area at the depth of the crack tip, the stress level of σ_{xx} is lower compared to the surface. The presence of crack #3 (see Fig. 9, row 4) increases the stress locally to approximately 50 % of the maximum stress at the surface in the undamaged case (see Fig. 12). A comparison of the shear stresses τ_{xy} around the tip of crack #3 between the undamaged (see Fig. 10) and the damaged case (see Fig. 11) confirms the local stress raise. This effect increases the proneness to crack propagation at the tip of crack #3.

Another finding is that the maximum compressive stress σ_{xx} below the contact increases by 10 % for the damaged case (see Fig. 12). This

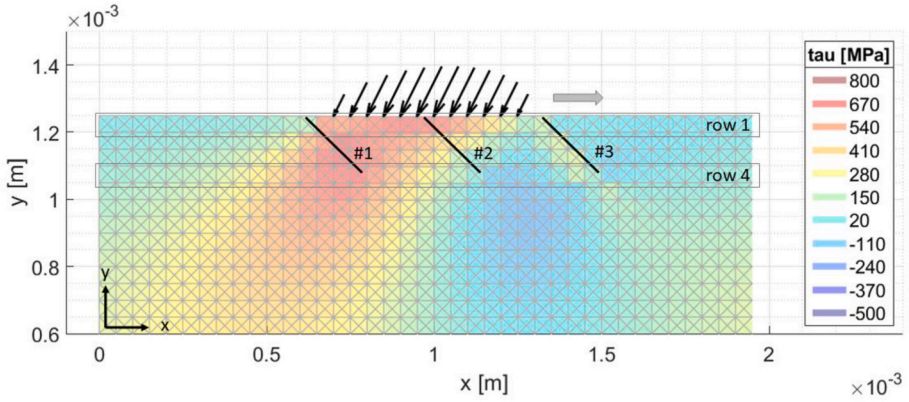

Fig. 11. Rolling contact simulation with shear stress distribution τ_{xy} that is subject to three surface cracks (displayed in black).

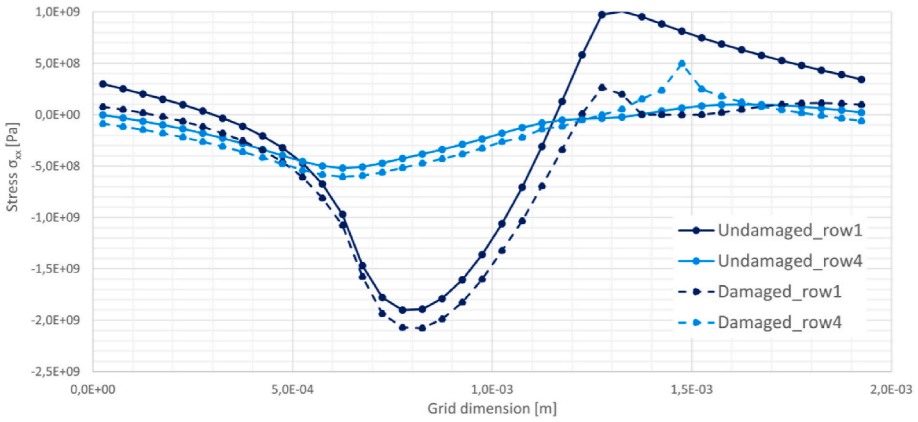

Fig. 12. Stresses σ_{xx} of surface- (row 1) and subsurface (row 4) layers: Solid lines refer to the undamaged-, the dashed ones to the damaged case.

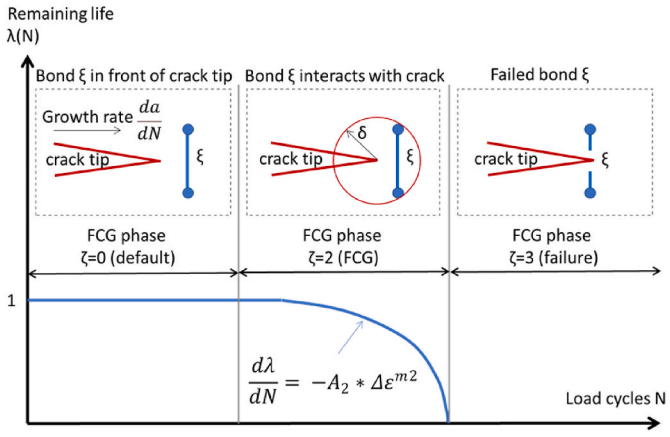

Fig. 13. Fatigue law and FCG activation: In case that a bond ξ is within the horizon δ of a crack tip, the fatigue law is activated (phase $\zeta = 2$), which reduces the remaining life $\lambda(N)$ per cycle N as a result of the fatigue law until failure occurs (phase $\zeta = 3$). The figure is modified from Ref. [8].

cannot be attributed to a single crack, but to the cluster of all three cracks.

In this way, the FCS bond law was applied to model the stress field around three initial cracks for a static condition, which delivered reasonable results. In the next step, a fatigue crack growth capability was introduced.

4. Fatigue crack growth

The fatigue crack growth capability was designed to simulate FCG as a result of multiple rolling contacts. An isotropic FCG behaviour of the material was assumed, and an initial crack was introduced. The fatigue law of Silling and Askari [8], which is the standard approach for peridynamic models applied to fatigue and RCF simulation [4,16,17], was adopted to the DEM model.

The fatigue law is based on the assumption that an FCG phase ζ is assigned to each element (see Fig. 13), which specifies the state of fatigue. For phase $\zeta = 0$ (default), the fatigue law is inactive, for phase $\zeta = 2$ (FCG), the fatigue law is enabled (FCG activation), and for $\zeta = 3$, the element is failed (failure). Regardless of the bond law, failure ($\zeta = 3$) implies that tension is not sustained anymore by the element (see Fig. 2). Within the scope of this work, crack initiation was not considered. Thus, the crack initiation phase of $\zeta = 1$ was neglected.

A horizon δ was set in a way that all bonds attached to a node were covered. For a failed bond (crack tip), the associated nodes were identified. The FCG activation was set to capture all bonds radially attached to these nodes and the bond phases were set to $\zeta = 2$. As a result, cracks can grow and branch along existing cracks.

The degradation itself was described by a property called remaining life, λ [0,1], that decreased as a result of the applied strain per load cycle, N (see Fig. 13).

$$\frac{d\lambda}{dN} = -A_2 * \Delta\varepsilon^{m_2} \qquad \text{Equation 3}$$

For $\lambda \leq 0$, an element fails, which was assumed to be irreversible. The reduction of λ was captured by the bond fatigue law (see Equation (3)), which is driven by the cyclic bond strain, $\Delta\varepsilon$, i.e. the difference between

Table 1
Parameter set for the mode I test.

Parameter	Value
A_2	1800
c_{el}	8.0e+6 N/m
l_0	5e-5 m
m_2	3.0

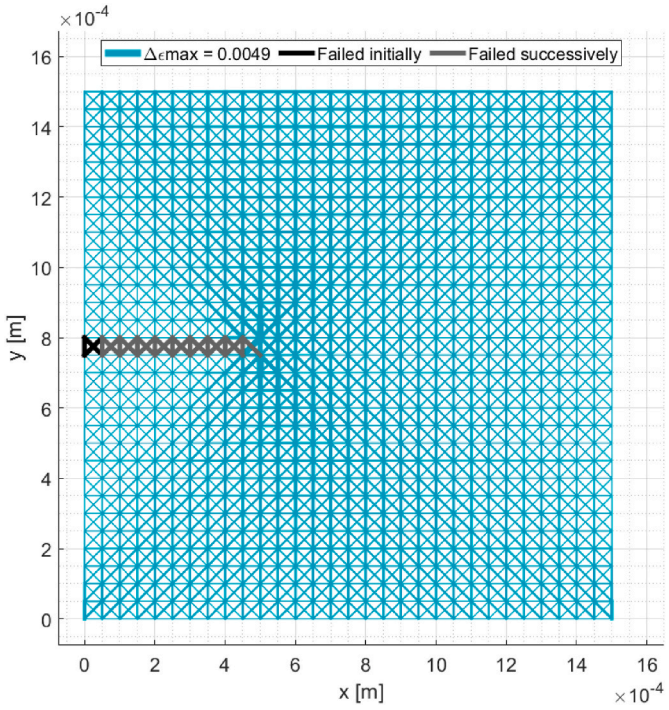

Fig. 14. FCG mode I simulation: The cyclic bond strain $\Delta\varepsilon$ per element is coloured in turquoise, initially failed elements in black, successively failed elements in grey.

the maximum and the minimum strain per load cycle.

$$\Delta\varepsilon = |\varepsilon_{max} - \varepsilon_{min}| \quad \text{Equation 4}$$

The fatigue law works with two fatigue parameters (A_2, m_2). The exponent m_2 corresponds to the exponent, m, of the Paris law. Thus, m_2 can be adopted directly from the slope of phase II of an experimental FCG diagram. For a detailed explanation of the derivation, the reader is referred to Silling and Askari [8].

$$m_2 = m \quad \text{Equation 5a}$$

The parameter A_2 can be derived by a calibration procedure with respect to a known, arbitrary value, A' and the associated crack growth rate, $\left(\frac{da}{dN}\right)'$. With these two parameters, the calibrated rate, $\left(\frac{da}{dN}\right)$ can be derived. For more details, the reader is referred to the work of Silling and Askari [6].

$$A_2 = A' \frac{da/dN}{(da/dN)'} \quad \text{Equation 6a}$$

The fatigue model does not depend on the processing of a stress intensity factor as in the classic linear-elastic fracture mechanics (LEFM). A consequence of the definition of the cyclic bond strain, $\Delta\varepsilon$ (see Equation (4)) is that for a mode I test, $\Delta\varepsilon$ can be calculated easily as there are just two values of strain, one for the minimum and one for the maximum load.

In order to test the FCG capability, a mode I test was performed for a 1.5 × 1.5 mm grid of steel material ($E = 210$ GPa, $\nu = 0.3$). The grid was discretised by a 30 × 30 grid with a basic element length of l_0 (see Table 1). A fixed boundary condition was applied to the bottom nodes of the grid.

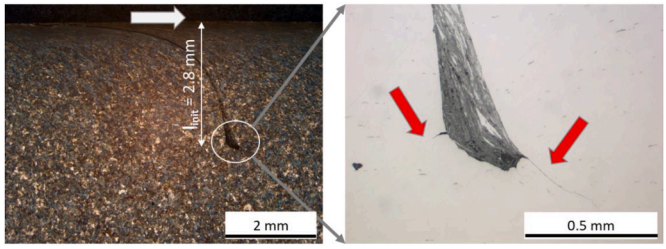

Fig. 15. Results from a full-scale test rig (courtesy of voestalpine Rail Technology GmbH): Section with initial crack (left) and magnification of the crack tip (right). The running direction is marked (left).

A cyclic tensile loading with a maximum stress of 300 MPa and a stress ratio of $R = 0.1$ was applied. The fatigue parameters (A_2,m_2) were not yet parametrised. As a starting point, parameters from Silling and Askari [8] were adopted (see Table 1). The FCS bond law (see Fig. 2a) was applied. Three initially failed elements (see Fig. 14, one vertical and two diagonals on the left edge) were set as an initial condition ($\zeta = 3$). A summary of the applied parameters is presented in Table 1.

The result of the simulation is displayed in Fig. 14. Starting from the three initially failed elements on the left edge (see Fig. 14, black bonds), the crack proceeds steadily to the centre (see Fig. 14, grey bonds). There are no horizontal outliers. The quality of the FCG behaviour is as expected and observed in experiments of rail steels in an undeformed state under similar stress ratios R, which were performed by Leitner et al. [2].

The cyclic bond strain $\Delta\varepsilon$ for healthy bonds is illustrated with respect to the maximum cyclic bond strain $\Delta\varepsilon_{max}$. The latter occurs directly in front of the crack (see Fig. 14, bold turquoise lines), which drives the crack growth (see Equation (3)). A close look on the DEM module in front of the crack (see Fig. 14) indicates that the module is strained in tension during the whole load cycle. In this case, the failed bonds are loaded in tension. Thus, the type of applied bond law does not play a role, as the bond laws differ in compression only.

5. RCF model

In the next step, the FCG capability was applied to a rolling contact model to simulate RCF. Thus, a load cycle was defined to incorporate all increments. The minimum- and maximum strains (ε_{max}, ε_{min}) were determined in an accumulative way per load cycle. This dictated that the update of the fatigue state (ζ, λ) must be performed in the post-processing of a cycle.

Isotropic FCG was assumed. As a reference for RCF in an undeformed material, the result of a full-scale test rig was adopted (see Fig. 15). A driven wheel was applied to a rail of virgin material. Initially, a cut of $l_{init} = 2.8$ mm depth was introduced, and no sharp tip was prepared. Then the rig was run for several rolling contact passes, where a normal load of 150 kN was applied. The normal contact stress, p_0 was estimated to yield 555 MPa. The coefficient of friction of the test was estimated to be $\mu = 0.3$.

The cyclic loading caused a plastic shear deformation above of the initial crack tip. However, the tip is still located in the quasi-undeformed material (see Fig. 15, left). A magnification reveals that there are two cracks branching from the bottom of the cut. A primary crack proceeds to the right in direction of the applied load, whereas a secondary crack branches to the left (see Fig. 15, right, red arrows).

The DEM model was set-up by a 57 × 25 grid. The discretisation was defined by a unit length of $l_0 = 0.5$ mm. The cut, i.e. initial crack, was modelled by an array of six modules, whereas horizontal- and diagonal bonds were selected (see Fig. 16, black bonds). This discretisation led to a crack length that was 7 % longer than that of the reference, which was

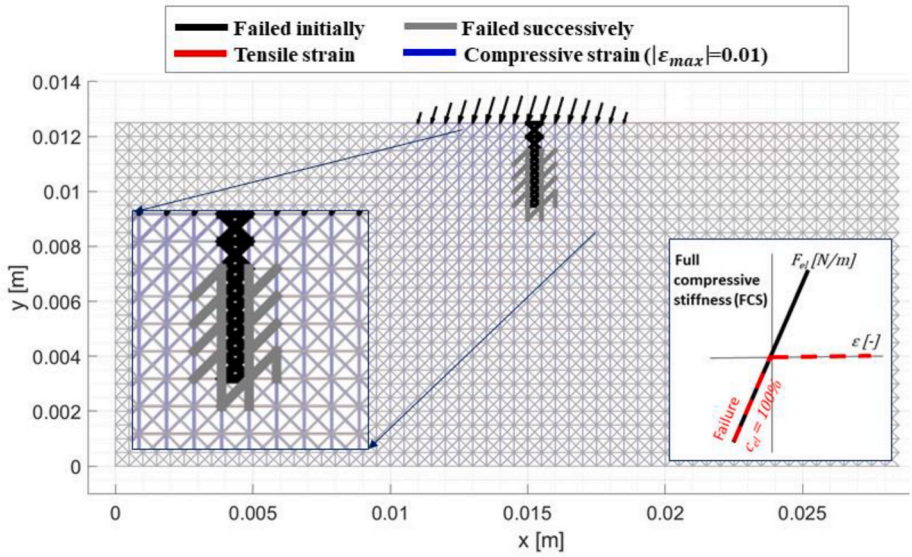

Fig. 16. RCF simulation for the FCS bond law (see subfigure right). The strain field is visualised by the line width, normalised to the magnitude of the maximum bond strain, $|\boldsymbol{\varepsilon}_{max\_init}| = \mathbf{0.01}$.

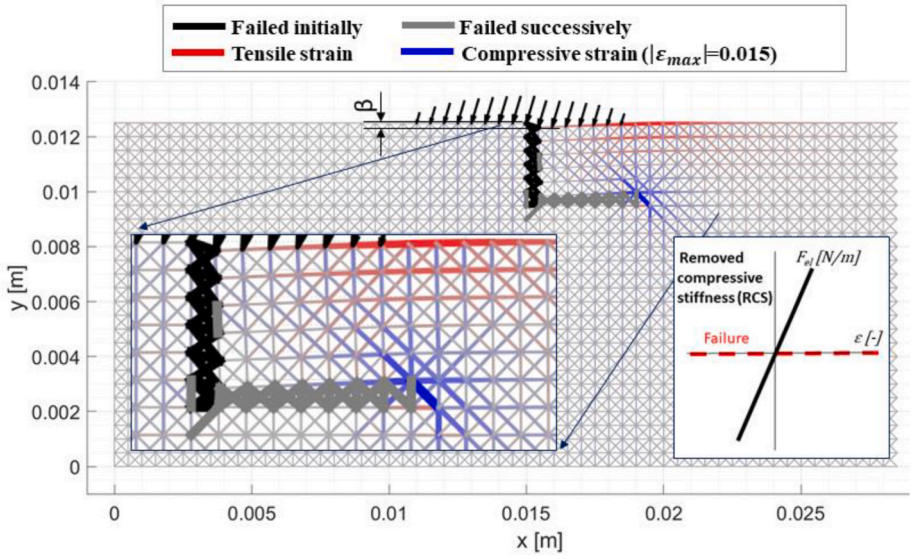

Fig. 17. RCF simulation for the RCS bond law (see subfigure right). The strain field is visualised by the line width, normalised to the magnitude of the maximum bond strain, $|\boldsymbol{\varepsilon}_{max\_def}| = \mathbf{0.015}$.

seen to be negligible.

For peridynamic models and DEM models of solid materials, a surface effect occurs due to the fact that nodes on the surface are attached to less elements than within the bulk material. This leads to an artificial softening of the surface layer, which is detailed by Le and Bobaru [18]. For this reason, and in order to study the fatigue development around the crack tip, the FCG capability of the elements associated to the first two rows of surface modules was disabled ($\zeta = 0$).

The RCF model was set to run for the FCS bond law, i.e. full stiffness for failed bonds loaded in compression (see Fig. 2a), and for the RCS bond law, i.e. zero stiffness for failed elements (see Fig. 2b). The result for the FCS bond is displayed in Fig. 16. The cyclic loading leads to a column-type cluster of failed elements which is centred around the initial crack. Only elements of the first two rows do not fail, as failure was disabled for these. However, no directed FCG occurred, i.e. a crack that propagates along a specific crack tip, which was observed in the experimental study (see Fig. 15).

The reason for this effect is the homogeneous strain field around the crack (see Fig. 16, equally sized compressive strains), which results from the stiff FCS bond law. Although Fig. 16 displays only one increment, it is representative for the whole load cycle. Due to the rolling contact, most elements are strained in compression. In combination with the FCS bond law (see Fig. 2a), this implies that the strain field resembles that of a grid without a crack. Thus, the strain distribution does not deviate significantly for different increments of one cycle. A consequence of the homogeneous strain field is that there is no distinctive maximum of $\Delta\varepsilon$ where the crack can proceed. This makes the set-up inappropriate to capture the RCF behaviour observed in the rig test (see Fig. 15).

The RCS bond law delivered a different FCG pattern (see Fig. 17). The crack proceeds along a straight path to the right, i.e. in direction of the rolling contact. This is in general agreement with the primary crack of the experimental reference (see Fig. 15). An analysis of the strain field for the increment reveals two distinctive strain maxima, a tensile one on the surface and a compressive one close to the primary crack tip (see

Fig. 17). Obviously, the latter drives the crack propagation. The former has no direct effect due to the initial condition.

The RCS bond law with no stiffness in compression leads to an unrealistically high displacement (lowering) of the surface above the crack (see Fig. 17). The bond law interrupts the load path across the elements of the crack, which leads to an unloading of the material below the crack (see Fig. 17). This distortion of the strain field implied by the RCS bond law is likely to have a detrimental impact on the FCG development.

These findings suggest that the RCS bond law is an appropriate starting point for RCF modelling as it facilitates a directed FCG. A drawback of the bond law set-up, however, is the potential occurrence of excessive grid deformation, which results in non-physical effects. Moreover, crack closure effects are expected to play an important role (see Fig. 3) and need to be considered. Thus, an alternative set-up is required to mediate between the two set-ups (see Fig. 2a and b).

6. Crack closure

In order to answer the question "how to model cracks loaded in compression", highlighted by the example of a loaded specimen (see Fig. 1) and the RCF model (see Fig. 17), a novel approach between the FCS - and the RCS bond laws is required. Experimental results of crack closure studies (see Fig. 3) provide a reference to calibrate the bond law, which is pursued here.

By crack closure, the interaction between two crack faces is meant. For a tensile load, this results in a retarded opening, which implies a shielding of the crack. However, the phenomenon is complex, and different mechanisms like plasticity-induced closure (PICC) or roughness-induced closure (RICC) were identified [13]. In this work, the macro-mechanical crack closure behaviour under a compressive load is modelled. The developed method represents an initial approach, which is based on several assumptions: No specific closure mechanism, but the macro-mechanical response is modelled; For cyclic hardening materials like Pearlitic steels, PICC is assumed to be the dominant mechanism, RICC plays a minor role [19]; Around the crack tip, a plane strain condition is assumed [20]; LEFM is assumed to be applicable around the crack tip to calculate the COD [21]; The microstructure influence was neglected; Due to the limited availability of test data, the closure behaviour of Ck45 steel was adopted to model pearlitic rail steel; In this way, the load-COD curve (see Fig. 3) was modelled for different bond law set-ups (see Fig. 4c) and compared to an experimental result for calibration.

Traditionally, crack closure was investigated for purely tensile conditions [13]. However, there are applications as the wheel-rail interaction where the compressive regime is dominant. For these conditions, fatigue crack growth was investigated by Fleck et al. [22] and Hermann et al. [23]. Their findings suggest that fatigue cracks could grow under a purely compressive load, if a plasticity induced residual stress field around the crack tip is present. This is assumed here.

Crack closure is characterised by the opening load P_{open}, i.e. the load at which the crack is fully open. However, experimental results indicate that a clear distinction of the opening load is challenging to obtain (see Fig. 3). This is complicated by the fact that there are several methods to derive P_{open}, which tend to lead to diverging results [20]. Thus, results for opening loads must be considered carefully.

Romeiro et al. [24] and Silva [19] performed studies on FCG and crack closure under negative stress ratios R for Ck45 structural steels. Both studies indicate that the opening load depends on the stress ratio R, which results in negative opening loads for $R < 0$, i.e. the crack is fully open under a compressive load. Vice versa, tensile conditions of $R > 0$ promote positive opening loads. This suggests that under a rolling contact condition, negative opening loads $P_{open} < 0$ can be assumed.

The goal of the calibration is to capture the macro-mechanical load-displacement behaviour for different loading conditions in order to set-up an appropriate bond law. This means that tension-compression tests

Table 2
Opening loads P_{open} as a function of the stress ratio R, modified from Romeiro et al. [24].

R [−]	P_{max} [kN]	P_{open} [kN]	P_{open}/P_{max}
−3	30	−5	−0.17
−2	40	−3	−0.08
−1	80	−8	−0.10
−1	40	0	+0.00
0	30	4	+0.13

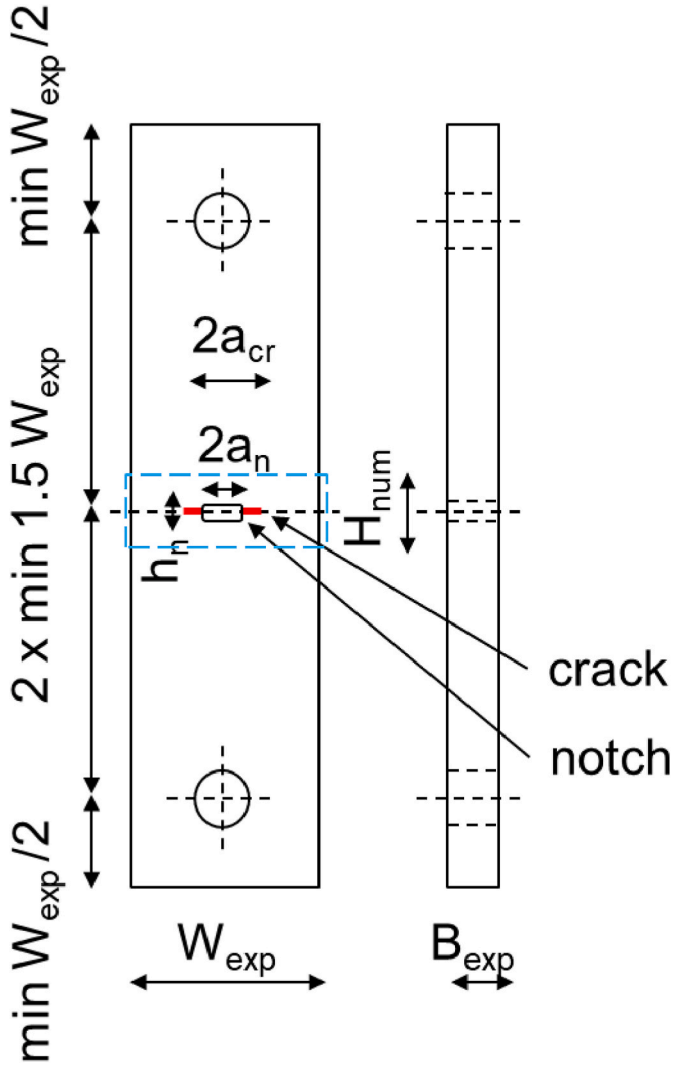

Fig. 18. Dimensions of the MT specimen, modified from Ref. [25]. The modelled cut-out is marked by the blue frame. (For interpretation of the references to colour in this figure legend, the reader is referred to the Web version of this article.)

are modelled, the COD is simulated and the resulting load-COD diagram (see Fig. 3) is illustrated. Therefore, a reference case was required. With respect to the rolling contact regime, the result for $R = -3$ was selected from Romeiro's study [24] (see Table 2).

A middle-crack tension (MT) specimen was modelled with respect to the study [24] and the ASTM standard E647 [25]. The main dimensions are defined by the width, $W_{exp} = 43$ mm and the thickness, $B_{exp} = 10$ mm. A central notch of length $2a_n = 6$ mm and height $h_n = 0.25$ mm and a pre-cracking were applied, resulting in a total length of $2a_{cr} = 10$ mm (see Fig. 18).

The discretisation of the model was performed with reference to the

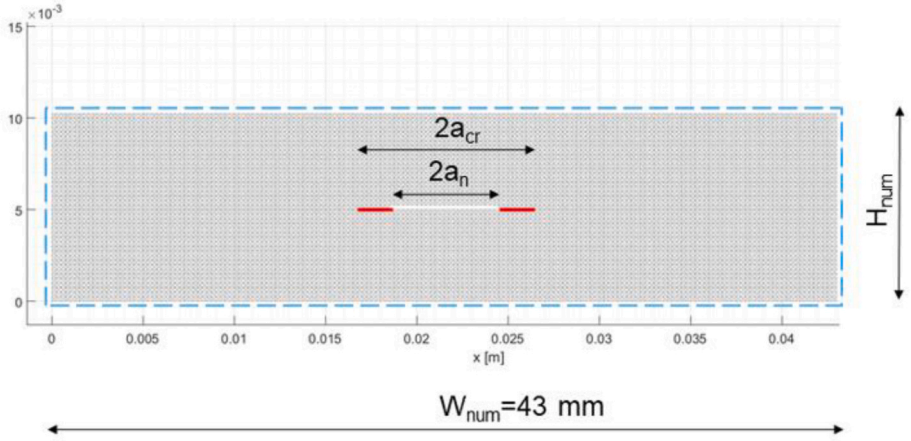

Fig. 19. Model of the MT specimen with a notch and a pre-crack (red). The blue frame refers to the cut-out of Fig. 18. (For interpretation of the references to colour in this figure legend, the reader is referred to the Web version of this article.)

Table 3
Coefficients of the smoothed bond law applied for the calibration.

Parameter	Value
c_{el}	3.89e+7 N/m
f_{poly}	1.5
n_{poly}	3.0

notch height h_n, resulting in a unit length of $l_0 = 0.25$ mm. In order to make the simulation more efficient, a cut-out of the specimen with a height of $H_{num} = 10.25$ mm was modelled (see Fig. 18). This resulted in a 172 × 41 grid (see Fig. 19). A floating boundary condition was applied to the bottom nodes. The discretisation was checked for potential edge effects, but none were identified. Finally the COD was modelled, which was defined by the vertical centreline displacements between the top- and bottom nodes of the notch, which is in accordance with the ASTM standard [25].

Regarding the bond law layout, the concepts of Fig. 4 were assessed. As the objective was to obtain full stiffness for a fully closed crack (see Fig. 3), the reduced elasticity set-up (see Fig. 4a) was deemed to be inappropriate. Thus, the bond law with the strain offset (see Fig. 4b) was preferred, which required one parameter, ε_{off} to be defined. Due to numerical reasons, however, the offset was smoothed by a polynomial approximation, described by the coefficient n_{poly}, between $\varepsilon = 0$ and the final strain, ε_{final} (see Fig. 4c), which is characterised by a polynomial factor, f_{poly}.

$$\varepsilon_{final} = f_{poly} * \varepsilon_{off} \qquad \text{Equation 5b}$$

Both coefficients n_{poly} and f_{poly} were set in an empirical way (see Table 3). This represents an initial approach. With it, the bond force in case of failure F_{el_f} was established as a function of a force associated to the final strain, F_{el_final}.

$$F_{el\_f} = \begin{cases} 0 \quad for\ \varepsilon \geq 0 \\ F_{el\_final}\left(\dfrac{\varepsilon}{\varepsilon_{final}}\right)^{n_{poly}} \quad for\ \varepsilon_{final} \leq \varepsilon < 0 \\ F_{el\_final} + c_{el}\left(\varepsilon - \varepsilon_{final}\right) \quad \text{for } \varepsilon < \varepsilon_{final} \end{cases} \qquad \text{Equation 6b}$$

$$F_{el\_final} = c_{el} * \left(\varepsilon_{final} - \varepsilon_{off}\right) \qquad \text{Equation 7}$$

The same set-up was employed to the RCF model (see section 5) for offset strains of $\varepsilon_{off} = -4\%$, $\varepsilon_{off} = -6\%$ and $\varepsilon_{off} = -10\%$. The results for $\varepsilon_{off} = -4\%$ indicated a clustered FCG pattern, comparable to Fig. 16. This suggested that the offset is too low, which resulted in a behaviour similar to that of failed bonds with full stiffness in compression. Thus, only the offsets, $\varepsilon_{off} = -6\%$ and $\varepsilon_{off} = -10\%$ were employed for the calibration.

In order to process a load-COD curve (see Fig. 3) for the selected reference case (see Table 2), load points in the range from the maximum tensile load, P_{max} to the maximum compressive (minimum) load, P_{min}, including the opening load, P_{open}, were simulated (see Fig. 20). For the maximum load, stress maxima occur at the crack tips (see Fig. 20, top). For the opening load, P_{open}, no significant stress concentrations occur (see Fig. 20, centre). For the minimum load, P_{min}, stress concentrations are present not only at the crack tips, but also around the crack mouths (see Fig. 20, bottom). It is remarkable that not even for P_{min}, which is multiple times higher than P_{open}, the crack is fully closed. A consideration of a real crack subject to PICC, though, would reveal a similar phenomenon. Asperities on the crack faces wedge and impede a full closure of the crack, even for highest compressive loads. Thus, the model's result is in general agreement with the physical behaviour.

Finally, the load-COD curve was assessed. The reference results consist of a series of shifted curves. Romeiro et al. attributed these to the ongoing plastification of the material [24]. Thus, the curves with the minimum- and the maximum COD development were integrated to the load-COD diagram, as well as the simulation results (see Fig. 21). For high tension at P_{max}, it can be seen that the simulation results diverge from the experimental behaviour, which is observed to a lesser degree for high compressive loads at P_{min} as well. In the range of moderate loads between P_{open} and P_5, however, the simulation agrees with the experiment. This is attributed to the linear-elastic layout of the model, which does not consider plastification.

In order to check this assumption, the equivalent stress maxima were assessed for each load point (see Table 4). These were compared to the yield stress of the Ck45 steel, which was reported to be $\sigma_y = 350$ MPa [24]. In the tensile regime of the load-COD figure (see Fig. 21), yielding seems to start already before the maximum load, P_{max}, as the experimental curves already drift for P_2. Regarding the compressive regime, the simulation predicts an exceeding of the yield limit for the range of P_6 to P_{max} (see Table 4). This explains the progressing drift between the experimental- and the simulation results. In this way, the linear-elastic range was defined from P_{open} to P_5, for which a calibration of the bond law is permitted (see Fig. 21).

Within the linear-elastic range, the model behaves slightly stiffer than the experiment. This may be attributed to the model's inherent limitation to a Poisson ratio of $\nu = 0.25$ [15], which limits the lateral expansion and contraction during compressive- and tensile loading. As a result, the crack's COD will displace less, which is illustrated in Fig. 21. This characteristic cannot be overcome. However, its effect can be

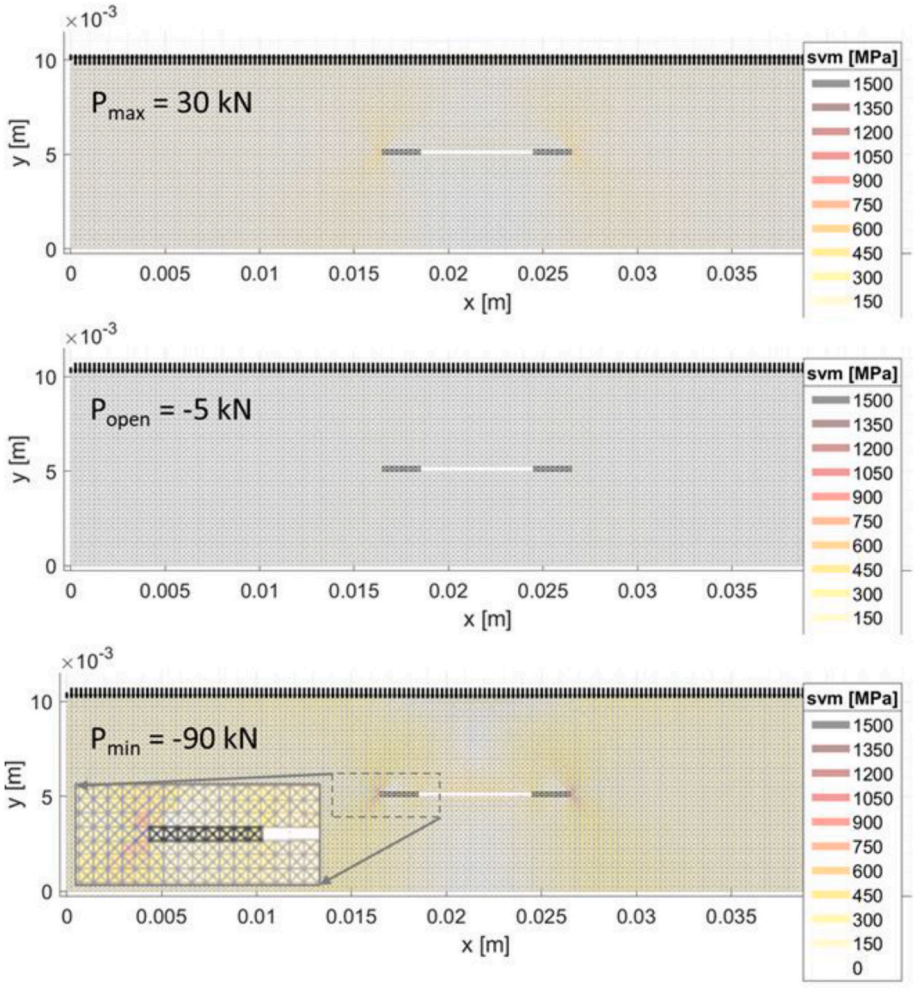

Fig. 20. Results for the maximum- (top), opening- (centre) and minimum loads (bottom). For the minimum load case, a magnification around the crack (black elements) is displayed. The results refer to $\varepsilon_{off} = -10$ %.

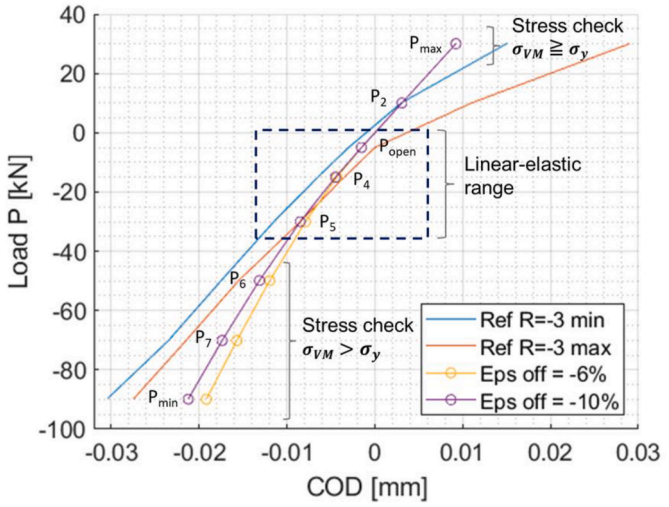

Fig. 21. Load-COD diagram for the minimum- and maximum experimental reference cases, and the simulation results for two bond law set-ups ($\varepsilon_{off} = -6\%, \varepsilon_{off} = -10\%$).

slightly reduced by the softer bond law of $\varepsilon_{off} = -10\%$. A further reduction of the offset was not considered in order to prevent excessive surface lowering of the RCF model. For this reason, the set-up $\varepsilon_{off} = -10\%$ was adopted (crack closure bond law, "CC").

Table 4
Maximum Von Mises σ_{VM} stresses per load point.

	P [kN]	σ_{VM} [MPa]
P_{max}	30	327
P_2	10	109
P_{open}	−5	54
P_4	−15	158
P_5	−30	293
P_6	−50	443
P_7	−70	572
P_{min}	−90	685

Finally, the initial assumption of $R = -3$ was checked. The stress ratio R was defined for a uniaxial tension- or compression load, not for a multiaxial loading as in the rolling contact. Thus, an equivalent stress ratio R_{eq} was defined by means of the principal stresses σ_1 and σ_2.

$$R_{eq} = \frac{\sigma_2}{\sigma_1} \qquad \text{Equation 8}$$

Then, the RCF model with the crack closure bond law was set up and run for one cycle. The stress tensors were post-processed per DEM module, and the equivalent stress ratios R_{eq} derived. The results indicated that all ratios were negative. On the surface row, they were in a range of $R_{eq} = -2$ to $R_{eq} = -50$. For the rows below the surface, the ratios decreased to a range of $R_{eq} = -12$ to $R_{eq} = -300$. Thus, the

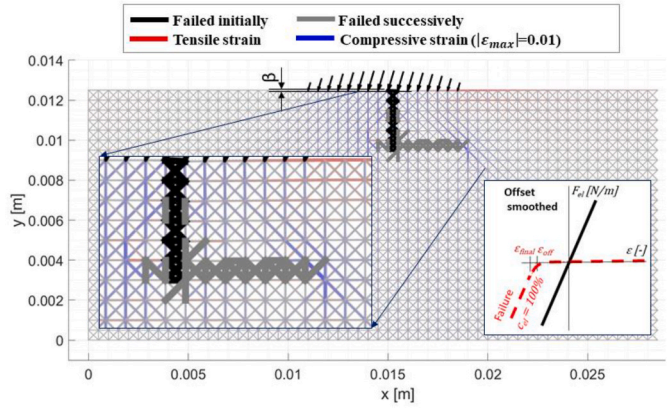

Fig. 22. RCF simulation for the crack closure bond law (see subfigure right). The strain field is visualised by the line width, normalised to the magnitude of the maximum bond strain, $|\boldsymbol{\varepsilon}_{max\_cc}| = \mathbf{0.01}$.

initial assumption of $R = -3$ is justified.

In this way, a novel calibration procedure was defined to derive an improved bond law referenced to crack closure. The phenomenon of crack closure is complex, and simplifications had to be assumed. The calibration is valid for the linear elastic range. Within that range, the calibration delivers a satisfying result for the bond law with smoothed offset (see Fig. 4c), which was applied to the RCF model.

7. RCF and crack closure

In the next step, the RCF model (see section 5) was run with the crack closure bond law (see Fig. 4c) for $\varepsilon_{off} = -10\%$. In order to assess the impact of the novel bond law, the strain field (see Fig. 22) is compared to that of the RCS set-up (see Fig. 17) for a comparable crack length. As the magnitudes of the strain maxima diverge significantly, individual strain references were applied.

The crack closure bond law leads to a stiffening of the grid in the vicinity of the crack. For the same applied contact stress, the maximum strains at the surface and around the crack tip reduce by a factor of 4. However, the quality of the strain distribution around the crack tip of the novel set-up resembles that of the RCS one (see Fig. 17), which causes a similar crack pattern (see Fig. 22).

A key aspect is that for the crack closure bond law, the surface lowering is minimised from $\beta_{RCS} = 0.16$ mm (see Fig. 17) to $\beta_{CC} = 0.05$ mm (see Fig. 22). The analytical ("an") solution for a Hertzian contact without crack gives a lowering of $\beta_{an} = 0.065$ mm. This means that the lowering of the model for the crack closure bond law equals 76 % of that from the analytical reference, which is attributed to the model's reduced Poisson ratio [15]. However, the approach from the literature (RCS bond law) results in a lowering that approximates 250 % of the analytical solution, which highlights the requirement for a stiffening of the bond law in case of failure.

A major difference regards the strain field to the left of the initial crack. The crack closure bond law facilitates a certain load transfer across the crack, which is manifested in the compressive strain field to the left of the initial crack (see Fig. 22). This is also valid for the area below the successively failed crack, but not for the same area of the RCS case, where failed elements act like a void (see Fig. 17). This represents a major improvement of the crack closure bond law, as a load transfer across a crack under compression is facilitated. Furthermore, the risk of an interpenetration of the crack faces, as described by Freimanis and Kaewunruen [4], is eliminated.

The primary crack proceeds in the direction of the rolling contact (see Fig. 23). Moreover, a secondary crack branches from the initial crack tip to the left. Compared to the experimental reference (see Fig. 15, right), the model captures both cracks that branch from the initial tip and propagate in opposite directions. Further, there is indication for a third crack branching below the initial crack.

A drawback, though, is the geometric, directional FCG pattern as the primary crack proceeds on a strictly horizontal path. This is induced by the distribution of the cyclic bond strains $\Delta\varepsilon$ (see Fig. 23), which constrains the crack propagation. The effect of the distribution of $\Delta\varepsilon$, however, is governed by the FCG activation (see Fig. 13). A closer assessment of this set-up is considered to be key to improve the resolution of the FCG behaviour.

8. Conclusion & outlook

The developed DEM model is an efficient tool to simulate cracks under rolling contact conditions. As fatigue cracks can be modelled easily by failed bonds, multiple crack paths as well as branching and coalescence can be investigated. Another benefit is the numerical efficiency that enables the simulation of numerous contact cycles, which is important regarding RCF modelling.

Fatigue cracks grow as a result of cyclic loading, which is modelled by means of a bond-based damage law. In this way, the propagating cracks develop according to the local loading conditions of the bonds at the crack tip and the applied damage law.

A key issue for DEM- and peridynamic models employed to model

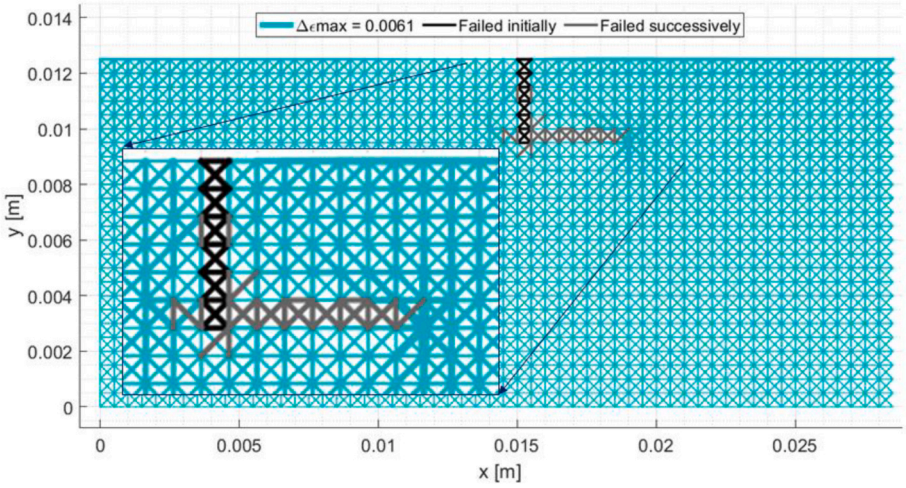

Fig. 23. RCF simulation for the crack closure bond law. The cyclic bond strain $\Delta\varepsilon$ per element is coloured in turquoise, initially failed elements in black, successively failed elements in grey.

rolling contacts is the behaviour of failed bonds loaded in compression. The standard approach is to remove the load carrying capability of a failed bond. For conditions where compressive loads prevail, this set-up reveals shortcomings due to a softening of the crack. This may lead to effects like excessive surface lowering, an interpenetration of crack faces and a distortion of the strain field.

The developed solution calibrates the bond law with respect to crack closure by the assignment of a moderate stiffness to failed bonds. This prevents artificial softening effects and facilitates directed FCG around a crack tip. A load transfer across a crack under compression is supported. The method delivers an important improvement for DEM- and peridynamic models where compressive loads dominate.

In the next stages of the model development, the fatigue capability will be assessed with respect to the tendency to directional FCG. Further, a parameterisation of the FCG behaviour will be performed for anisotropic rail materials and the applicability to the RCF model will be evaluated. Based on the findings, the damage law will be upgraded to account for the anisotropy of crack propagation which is associated to SPD.

CRediT authorship contribution statement

Markus Januschewsky: Conceptualization, Formal analysis, Methodology, Software, Validation, Visualization, Writing – original draft, Writing – review & editing. **Gerald Trummer:** Conceptualization, Formal analysis, Funding acquisition, Methodology, Project administration, Supervision. **Klaus Six:** Conceptualization, Formal analysis, Funding acquisition, Methodology. **Roger Lewis:** Conceptualization, Methodology, Supervision.

Declaration of competing interest

The authors declare that they have no known competing financial interests or personal relationships that could have appeared to influence the work reported in this paper.

Data availability

The authors do not have permission to share data.

Acknowledgments

This project has received funding from the Shift2Rail Joint Undertaking (JU) under grant agreement No 101012456. The JU receives support from the European Union's Horizon 2020 research and innovation programme and the Shift2Rail JU members other than the Union. The publication was written at Virtual Vehicle Research GmbH in Graz and partially funded within the COMET K2 Competence Centers for Excellent Technologies from the Austrian Federal Ministry for Climate Action (BMK), the Austrian Federal Ministry for Digital and Economic Affairs (BMDW), the Province of Styria (Dept. 12) and the Styrian Business Promotion Agency (SFG). The Austrian Research Promotion Agency (FFG) has been authorised for the programme management.

References

[1] G. Trummer, C. Marte, P. Dietmaier, C. Sommitsch, K. Six, Modeling surface rolling contact fatigue crack initiation taking severe plastic shear deformation into account, Wear 352–353 (2016) 136–145.
[2] T. Leitner, A. Hohenwarter, R. Pippan, Anisotropy in fracture and fatigue resistance of pearlitic steels and its effect on the crack path, Int. J. Fatig. 124 (2019) 528–536.
[3] G. Zhang, Q. Le, A. Loghin, A. Subramaniyan, F. Bobaru, Validation of a peridynamic model for fatigue cracking, Eng. Fract. Mech. 162 (2016) 76–94.
[4] A. Freimanis, S. Kaewunruen, Peridynamic analysis of rail squats, Appl. Sci. 8 (2299) (2018).
[5] P.A. Cundall, O.D.L. Strack, A discrete numerical model for granular assemblies, Geotechnique 29 (1) (1980) 47–65.
[6] L. Maheo, F. Dau, D. André, J.L. Charles, I. Iordanoff, A promising way to model cracks in composite using Discrete Element Method, Compos Part B 71 (2015) 193–202.
[7] L. Kosteski, I. Iturrioz, R.G. Batista, A.P. Cisilino, The truss-like discrete element method in fracture and damage mechanics, Eng. Comput. 28 (6) (2011) 765–787.
[8] S. Silling, A. Askari, Peridynamic model for fatigue cracks, SANDIA Rep SAND2014-18590 (2014) 1–40.
[9] S.A. Silling, E. Askari, A meshfree method based on the peridynamic model of solid mechanics, Comput. Struct. 83 (17–18) (2005) 1526–1535.
[10] M.A. Ghaffari, Multiscale Modeling and Simulation of Rolling Contact Fatigue, The University of Iowa, 2016.
[11] M.A. Ghaffari, S. Xiao, Peridynamic modeling and simulation of rolling contact fatigue, J. Appl. Mech. Eng. 6 (3) (2017).
[12] K. Kasaba, T. Sano, S. Kudo, T. Shoji, K. Katagiri, T. Sato, Fatigue crack growth under compressive loading, J. Nucl. Mater. 258–263 (1998) 2059–2063.
[13] T.L. Anderson, Fracture Mechanics - Fundamentals and Applications, third ed., Taylor & Francis Group, Boca Raton, FL, USA, 2005.
[14] K.L. Johnson, Contact Mechanics, first ed., Cambridge University Press, Cambridge, UK, 1987.
[15] S.A. Silling, M. Epton, O. Weckner, J. Xu, E. Askari, Peridynamic states and constitutive modeling, J. Elasticity 88 (2) (2007) 151–184.
[16] L. Wang, X. Sheng, J. Luo, A peridynamic damage-cumulative model for rolling contact fatigue, Theor. Appl. Fract. Mech. 121 (2022) 103489. June.
[17] X. Ma, L. Wang, J. Xu, Q. Feng, L. Liu, H. Chen, A two-dimensional ordinary state-based peridynamic model for surface fatigue crack propagation in railheads, Eng. Fract. Mech. (2022) 265. November 2021.
[18] Q.V. Le, F. Bobaru, Surface corrections for peridynamic models in elasticity and fracture, Comput. Mech. 61 (4) (2018) 499–518.
[19] F.S. Silva, The importance of compressive stresses on fatigue crack propagation rate, Int. J. Fatig. 27 (10–12) (2005) 1441–1452.
[20] S. Stoychev, D. Kujawski, Methods for crack opening load and crack tip shielding determination: a review, Fatig. Fract. Eng. Mater. Struct. 26 (11) (2003) 1053–1067.
[21] M.N. James, W.N. Sharpe, Closure development and crack opening displacement in the short crack regime for fine and coarse grained A533B steel, Fatig. Fract. Eng. Mater. Struct. 12 (4) (1989) 347–361.
[22] N.A. Fleck, C.S. Shin, R.A. Smith, Fatigue crack growth under compressive loading, Eng. Fract. Mech. 21 (1) (1985) 173–185.
[23] R. Hermann, Fatigue crack growth in ductile materials under cyclic compressive loading, Fatig. Fract. Eng. Mater. Struct. 17 (1) (1994) 93–103.
[24] F.F. Romeiro, C.A. Domingos, M.J. Freitas, Measurement for Fatigue Crack Closure for Negative Stress Ratio, vol. 1343, ASTM Spec Tech Publ - Adv Fatigue Crack Clos Meas Anal, 1999, pp. 321–336. Second.
[25] ASTM International, Standard Test Method for Measurement of Fatigue Crack Growth Rates - E647, 2019. West Conshohocken, PA, USA.